

¹ Contents

2	1 Diamond detectors for radiation detection	2
3	1.1 Semiconductor detectors	3
4	1.2 Principles of signal formation in semiconductors	4
5	1.2.1 Signal induction by moving charges	5
6	1.2.2 Shockley-Ramo theorem	7
7	1.2.3 Thermal excitation	7
8	1.2.4 Space charge	8
9	1.3 Carrier transport in a diamond sensor	8
10	1.4 Radiation-induced current signals	10
11	1.4.1 Mean energy loss	11
12	1.4.2 Signal fluctuation	11
13	1.4.3 Charge collection	12
14	1.4.4 Charge trapping	13
15	1.5 Radiation damage	14
16	1.6 Temperature effects	16
17	1.7 Electronics for signal processing	16
18	1.7.1 Signal preamplifiers	17
19	1.7.2 Analogue-to-digital converters	19
20	1.7.3 Digital signal processing	20

₂₁ **Chapter 1**

₂₂ **Diamond detectors for radiation
23 detection**

₂₄ Diamond has been known for over two millennia, valued for its mechanical properties and
₂₅ its appearance. When the procedures for its synthesis were discovered, diamond made its
₂₆ way to a broad range of industries which exploit its optical and electrical properties. The
₂₇ discovery of the Chemical Vapour Deposition (CVD, described below) as a new synthesis
₂₈ process gave rise to a range of new applications. Purer specimens are used in electronics,
₂₉ high-power switching devices, electrochemical systems, radiation sensors, quantum comput-
₃₀ ing etc. Recently it was found that it also exhibits superconductivity [1]. This thesis focuses
₃₁ on the use of diamond for radiation detection. An example of such a diamond sample is
₃₂ shown in figure 1.1.

₃₃ Compared to a natural diamond, a CVD diamond used as a particle detector has almost
₃₄ no impurities (foreign atoms like nitrogen or boron). If proper procedures are followed, the
₃₅ diamond lattice can be grown very uniformly. This in turn improves electrical properties
₃₆ of the grown sample. Such a diamond is an almost perfect thermal and electrical insulator.
₃₇ However, its electrical behaviour is similar to that of a semiconductor. For this reason this
₃₈ chapter first introduces semiconductor detectors and then describes the principle of signal
₃₉ formation in semiconductors. Then it focuses on the diamond sensor and its properties.

₄₀ **Chemical vapour deposition** (CVD) [2] is a process where a material is deposited from
₄₁ a gas onto a substrate, involving chemical reactions. It is often carried out under high
₄₂ pressure and high temperatures. It takes place in enclosed chambers called furnaces with
₄₃ careful regulation of the temperature, pressure and gas mixture. Synthetic diamond is
₄₄ grown at 700–900 °C with a mixture of hydrogen and methane gas. At this temperature the
₄₅ molecules dissociate into carbon and hydrogen atoms. The carbon atoms are the building
₄₆ blocks and are deposited on the surface of the substrate.

₄₇ Under a carefully controlled pressure and temperature conditions with an added abrasive
₄₈ atomic hydrogen the graphitic bonds break and form into diamond bonds. The speed of
₄₉ the growth can be anywhere between 0.1 and 10 µm per hour. The detector grade samples
₅₀ are grown at a rate of the order of 1 µm per hour. They can grow up to several millimetres
₅₁ in thickness. The width of the samples, however, depends entirely on the substrate used.

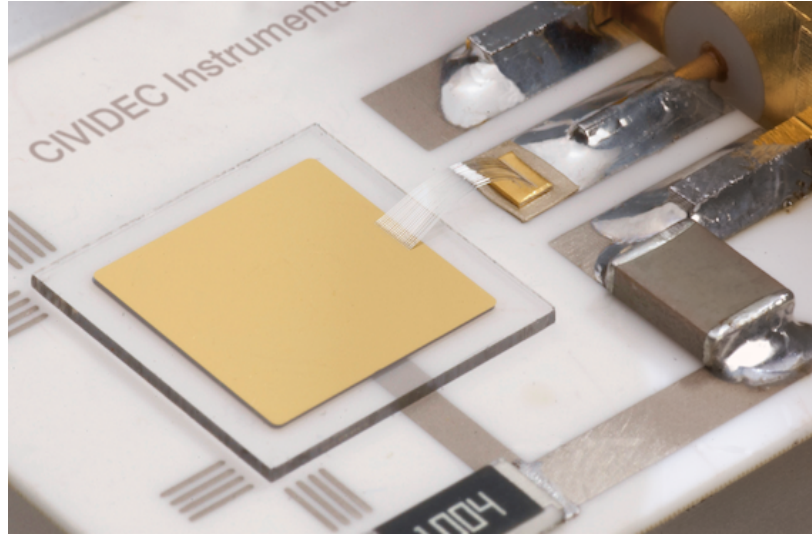


Figure 1.1: A pCVD diamond pad detector [3].

52 Diamond can be deposited on various materials: diamond, silicon, tungsten, quartz glass etc.
53 The substrate material must be able to withstand the high temperatures during the CVD
54 process. The diamond substrate does not need any surface pre-treatment. Carbon atoms
55 form bonds with atoms in the existing crystal structure. This is the homo-epitaxial growth
56 where the newly deposited atoms retain the orientation of the structure in the substrate.
57 Other non-diamond substrates, however, need to be pre-treated, usually by being polished
58 using diamond powder. Some powder particles remain on the surface, acting as seeds for
59 the growth of small crystals or grains. These grains grow and at some point merge with the
60 adjacent ones, making up a compact material. The lower side is later polished away. These
61 diamonds are called *polycrystalline* (pCVD) whereas those grown on a diamond substrate
62 are *single crystal* (sCVD) diamonds. The area of the former can be large - up to 0.5 m^2 or
63 more compact 75 cm^2 in the case of detector grade diamonds, which can be further cut into
64 smaller parts. The sCVD diamonds, on the other hand, can currently only achieve sizes up
65 to 1.5 cm^2 .

66 1.1 Semiconductor detectors

67 Semiconductor is a class of solids whose electrical conductivity is between that of a conductor
68 and that of an insulator – of the order of $10^{-5} \Omega^{-1} \text{ cm}^{-1}$. Semiconductors consist of
69 atoms with four electrons in their valence band, e.g. silicon–Si or germanium–Ge, or as
70 combinations of two or more different materials, e.g. gallium arsenide–GaAs). The atoms
71 in the lattice form valence bonds with adjacent atoms, creating solid crystal structures.

72 Semiconductor particle detectors are devices that use a semiconductor material to detect
73 radiation. They work on the principle of an ionisation chamber. An incident particle ionises
74 the atoms in the crystal lattice. The charges are freed if the deposited energy is higher than
75 the energy band gap, i.e. the energy needed to excite an electron from its steady state
76 to the conductance band. The freed charge carriers start drifting in an externally applied



Figure 1.2: The Insertable B-Layer – a silicon particle tracker installed in the ATLAS experiment in 2014 [5].

77 electric field, inducing current on the electrodes. The induced signal is amplified and read
78 out by the electronics in the detector signal chain.

79 Semiconductor detectors are most widely used for tracking applications, like the In-
80 sertable B-Layer shown in figure 1.2 [4], which was installed in ATLAS Experiment in 2014.
81 First, they can be produced in thin layers to minimise the impact on the path of the inci-
82 dent particles. Second, their low sensor capacitance allows for a fast signal response. Third,
83 they are highly efficient and highly resistant to radiation damage. Finally, the industrial
84 processes allow for a fine spatial segmentation, which in turn improves the track resolution
85 of the detector systems.

86 Semiconductor sensors come in several configurations. The simplest type is a pad – a
87 single plate with two electrodes. Pads are used for particle counting and radiation moni-
88 toring. Next is a strip detector, a more finely segmented detector made out of long parallel
89 sensing areas or strips. Normally each strip has its own signal line for readout. Usually the
90 strip detectors are used in pairs – one detector is placed on top of the other at an angle to
91 increase spatial resolution in both axes. The third and the most finely segmented is a pixel
92 detector, consisting of a 2D array of independent sensing areas. In tracking applications,
93 pixel detectors are used where the need for a high detection resolution and granularity re-
94 quirement is the highest. Due to their high production cost and a high number of signal
95 channels, they can only cover limited areas. Strip detectors can be used to cover larger
96 areas in several consecutive layers.

97 1.2 Principles of signal formation in semiconductors

98 Particles can interact with the sensor in several ways, e.g. via bremsstrahlung [6], elastic
99 or inelastic scattering or nuclear reactions [7]. Bremsstrahlung is radiation created when a
100 particle is decelerated due to interaction with the electric field of the core of an atom. Elastic

101 scattering is deflection of the particle's trajectory due to the pull from the nucleus without
 102 depositing any energy in it. This is in principle an unwanted effect in semiconductors as
 103 it deteriorates the spatial resolution of the sensor. Inelastic scattering is the interaction
 104 through which an electron in the atom is *ionised*. Nuclear reaction is the direct interaction
 105 between the incident particle and the core of the atom. All these effects are competing
 106 and are dependent on the particle's mass, momentum etc. The scope of this chapter is to
 107 discuss the ionisation mechanism in semiconductors.

108 The energy of the electrons forming valence bonds between atoms in the crystal lattice
 109 is within the *valence band* [8]. To break a bond and excite the electron into a *conduction*
 110 *band*, a sufficient energy has to be applied. The minimal energy required is equal to the
 111 energy band gap E_g of the semiconductor. Typical E_g values are 0.7 eV in Ge, 1.12 eV in
 112 Si and 1.4 eV in GaAs. Diamond with its 5.5 eV band gap is considered an insulator. The
 113 separation between the conductive and valence band is referred to as *forbidden gap* where
 114 no electron states can exist.

115 An electron excited into the conduction band leaves behind a positively charged ion
 116 with a vacancy – a hole – in its valence band, as shown in figure 1.3a. A free *electron-hole*
 117 *pair* is thus created. The free electron travels through the crystal until it is recombined
 118 with another hole. Similarly the positive charge of the hole attracts a bound electron in
 119 the vicinity, causing it to break from the current bond and moving to the vacancy, thus
 120 leaving behind a newly created hole. The process continues, making it look like the hole is
 121 traveling through the material [8].

122 Both the electron and the hole are referred to as *charge carriers*. Without an externally
 123 applied electrical field, they propagate in random directions. Therefore on average there is
 124 no overall motion of charge carriers in any particular direction over time.

125 However, if an external electric field is applied to the crystalline structure, the free
 126 electrons and holes drift toward the positive and negative potential, respectively, as shown
 127 in figure 1.3b. While drifting, the charges couple with the electrodes, inducing current in
 128 the circuit, which is explained by the Shockley–Ramo theorem below. Upon reaching the
 129 electrodes the charges stop inducing the current. The equivalent electrical circuit is shown
 130 in figure 1.3c.

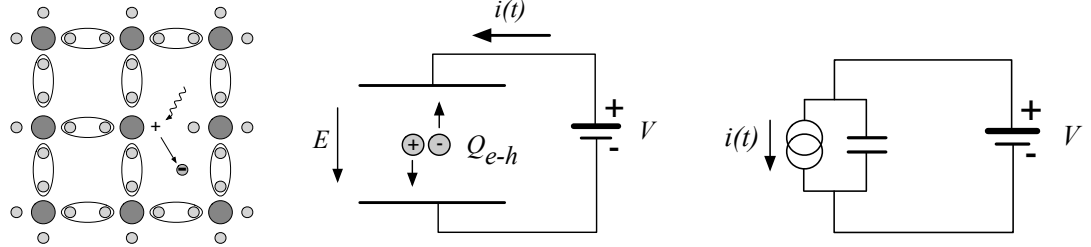
131 1.2.1 Signal induction by moving charges

132 The signal induction in a conducting plane by a point-like charge, which couples with
 133 an electrode, is derived in [9]. The electrode can in this case be modelled as an infinite
 134 conducting plane. When a point charge q is created (e.g. an electron-hole pair created
 135 via ionisation), its electrostatic field lines immediately couple with the electrode, as seen
 136 in figure 1.4a. The electric field on the metal surface due to a point-like charge q at the
 137 distance z_0 is

$$E_z(x, y) = \frac{q z_0}{2\pi\epsilon_0(x^2 + y^2 + z_0^2)^{\frac{3}{2}}} \quad E_y = E_z = 0. \quad (1.1)$$

138 A mirror charge appears on the conducting plane, with a charge density distribution

$$\sigma(x, y) = \epsilon_0 E_z(x, y) = \frac{q z_0}{2\pi(x^2 + y^2 + z_0^2)^{\frac{3}{2}}}. \quad (1.2)$$

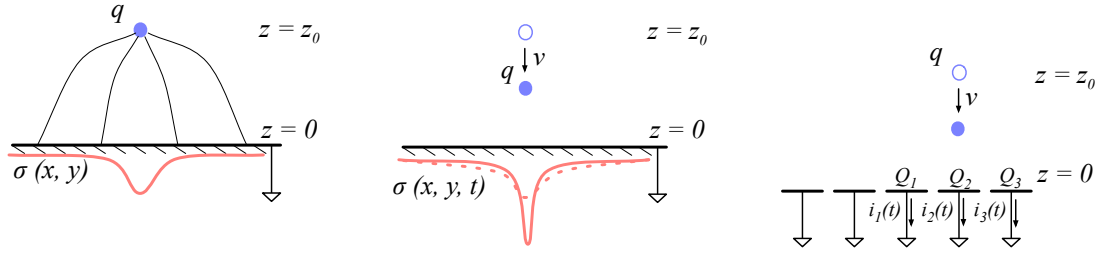


(a) Valence bonds in the crystalline structure can be broken, creating a free electron-hole pair

(b) The freed electron-hole pair starts drifting in the externally applied electric field. The electron and the hole both drift in the opposite directions towards the oppositely charged electrodes.

(c) Equivalent electrical circuit. The moving charges act as a current source.

Figure 1.3: In the equivalent electrical circuit diagram the electron-hole creation and drift can be modelled as a current source with a capacitor in parallel.



(a) Newly created point charge couples with the conductive plane.

(b) When the charge drifts, the charge density in the plane changes.

(c) The changing charge density in the small regions of the plane induces current.

Figure 1.4: A point-like charge inducing current in a conductive plane.

¹³⁹ The charge density integrated over the entire plane yields a mirror charge Q , which is an
¹⁴⁰ opposite of point charge q :

$$Q = \int_{-\infty}^{\infty} \int_{-\infty}^{\infty} \sigma(x, y) dx dy = -q. \quad (1.3)$$

¹⁴¹ The plane is then segmented into infinitely long strips with a width w whereby each of the
¹⁴² strips is grounded, as shown in figure 1.4c. Considering a charge density distribution 1.2, the
¹⁴³ resulting mirror charge on a single strip Q_2 directly below the point charge ($x = 0, y = 0$)
¹⁴⁴ yields

$$Q_2(z_0) = \int_{-\infty}^{\infty} \int_{-w/2}^{w/2} \sigma(x, y) dx dy = -\frac{2q}{\pi} \arctan\left(\frac{w}{2z_0}\right) \quad (1.4)$$

¹⁴⁵ If the charge starts moving towards the conducting plane, the mirror charge density distribution
¹⁴⁶ also changes, as shown in figure 1.4b. As a result the $Q_2[z(t)]$ changes with time.
¹⁴⁷ The changing charge is in effect an induced electric current $i_2(t)$:

$$i_2(t) = -\frac{d}{dt} Q_2[z(t)] = -\frac{\partial Q_2[z(t)]}{\partial z} \frac{\partial z(t)}{\partial t} = \frac{4qw}{\pi[4z(t)^2 + w^2]} v. \quad (1.5)$$

- 148 The movement of the point-like charge therefore induces current in the conducting plane.
 149 The induced current is linearly dependent on the velocity of the point-like charge.

150 **1.2.2 Shockley-Ramo theorem**

151 W. Shockley [10] and S. Ramo [11] independently proposed a theory which explains how
 152 a moving point charge induces current in a conductor. The Shockley-Ramo theorem can
 153 therefore be used to calculate the instantaneous electric current induced by the charge
 154 carrier or a group of charge carriers. It can be used for any number of electrodes. It states
 155 that the current $I_n^{\text{ind}}(t)$ induced on the grounded electrode n by a point charge q moving
 156 along a trajectory $\mathbf{x}(t)$ reads

$$I_n^{\text{ind}}(t) = -\frac{dQ_n(t)}{dt} = -\frac{q}{V_w} \nabla \Psi_n[\mathbf{x}(t)] v(t) = -\frac{q}{V_w} \mathbf{E}_n[\mathbf{x}(t)] v(t), \quad (1.6)$$

157 where $\mathbf{E}_n(\mathbf{x})$ is the *weighting field* of electrode n in the case where the charge q is removed,
 158 electrode n is set to voltage $V_w = 1$ and all other electrodes are grounded. The weighting
 159 field is defined as the spatial differential of the *weighting potential*: $\mathbf{E}_n(\mathbf{x}) = \nabla \Psi_n(\mathbf{x})$. In
 160 the case of two parallel electrodes, the weighting field is $E_w = -\frac{d\Psi}{dx} = -1/d$, where d is the
 161 distance between the electrodes. The resulting induced current is therefore

$$i(t) = \frac{q}{d} v_{\text{drift}}(x, t), \quad (1.7)$$

162 whereby v_{drift} is the drift velocity of the point-like charge and d is the distance between the
 163 electrodes. d is defined by the dimensions of the sensor. The drift velocity is a function
 164 of the externally applied electric field, as defined in section 1.3. If the electric field is set
 165 to a constant value, the induced current is directly proportional to the drifting charge.
 166 Therefore, by measuring the height of the induced current at a specific point of time the
 167 number of moving charges can be deduced.

168 **1.2.3 Thermal excitation**

169 Electrons can be thermally excited to the conduction band. The intrinsic concentration of
 170 thermally excited electrons n_i in semiconductors is proportional to[8]

$$n_i \propto \exp\left(-\frac{E_g}{2k_B T}\right) \quad (1.8)$$

171 wherein $k_B = 1.381 \times 10^{-23} \text{ m}^2 \text{ kg s}^{-2} \text{ K}^{-1}$ is the Boltzmann constant, E_g is the energy
 172 band gap of the semiconductor and T is the temperature in K. Due to the small band gap
 173 in semiconductors a significant amount of electrons already occupies the conduction band
 174 at room temperature due to thermal excitation, according to the probabilistic distribution.
 175 To reduce this effect semiconductor sensors are doped with donors and acceptors, forming
 176 a diode [8]. The diode is then inversely biased to deplete the material of all free charges.
 177 Doped silicon fulfills most of the needs for particle physics requirements and is therefore
 178 the most widely used material for particle detection. Diamond with its high energy band
 179 gap on the other hand only has a negligible number of thermally excited electrons at room
 180 temperature. Therefore a p-n junction is not needed, which simplifies the sensor production.

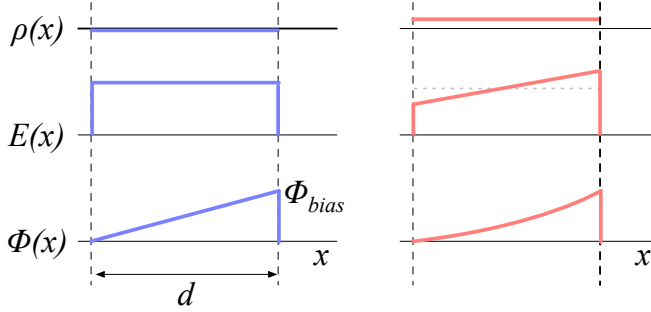


Figure 1.5: Left figure shows a profile of a diamond sensor only with an externally applied electric field. In the figure on the right a uniformly distributed space charge is added in the diamond, contributing to the internal electric field distribution. The induced current signal is proportional to the electrical field. d is the thickness of the diamond sensor.

¹⁸¹ **1.2.4 Space charge**

¹⁸² The Poisson equation shows that

$$\frac{d^2\Phi(x)}{dx^2} = \frac{dE(x)}{dx} = \frac{\rho(x)}{\epsilon} \quad (1.9)$$

¹⁸³ where $\rho(x)$ is the space charge distribution, E is the electrical field and Φ is the voltage
¹⁸⁴ potential. In an ideal diamond, the externally applied high voltage potential on the two
¹⁸⁵ electrodes decreases linearly through the sensor. The electrical field is therefore constant
¹⁸⁶ throughout the sensor and the space charge distribution across it equals 0. However, space
¹⁸⁷ charge may be introduced in the material either by means of accumulating of charge carriers
¹⁸⁸ in the lattice (i.e. charge trapping) or already during sensor production. The space charge
¹⁸⁹ can be either permanent or changing – sometimes it is possible to reduce it, as is shown
¹⁹⁰ in chapter ???. All in all, it is very important to reduce it because it affects the shape of
¹⁹¹ the electrical signal. Since the drift velocity of the charge carriers is proportional to the
¹⁹² electrical field, the charges change their velocity while drifting through the space charge
¹⁹³ region. Figure 1.5 compares the voltage potential, the electrical field and the space charge
¹⁹⁴ for an ideal sensor as well as for that with a uniformly distributed positive space charge.

¹⁹⁵ **1.3 Carrier transport in a diamond sensor**

¹⁹⁶ This section describes the carrier transport phenomena in diamond. This theory provides
¹⁹⁷ the basis for discussion about the measurements in chapter ???. Table 1.1 compares the
¹⁹⁸ properties of diamond and silicon. Some of these values are revisited and used in the course
¹⁹⁹ of this thesis.

Property	Diamond	Silicon
Band gap energy E_g (eV)	5.5	1.12
Electron mobility μ_e ($\text{cm}^2 \text{ V}^{-1} \text{ s}^{-1}$)	1800 [12]	1500 [8]
Hole mobility μ_h ($\text{cm}^2 \text{ V}^{-1} \text{ s}^{-1}$)	2500 [12]	450 [8]
Breakdown field (V cm^{-1})	10^7	3×10^5
Resistivity ($\Omega \text{ cm}$)	$> 10^{11}$	2.3×10^5
Intrinsic carrier density (cm^{-3})	$< 10^3$	1.5×10^{10}
Mass density (g cm^{-3})	3.52	2.33
Atomic charge	6	14
Dielectric constant ϵ	5.7	11.9
Displacement energy (eV/atom)	43	13 – 20
Energy to create an e-h pair (eV)	13	3.6
Radiation length (cm)	12.2	9.6
Avg. signal created/ μm (e)	36	89

Table 1.1: Comparison diamond – silicon [8, 12].

When the charge carriers are freed in a semiconductor with no concentration gradient and without an externally applied electric field, they scatter in random directions with a thermal velocity v_{th} [8]. Their integral movement due to thermal excitation equals zero.

Diffusion is caused by the concentration gradient. In its presence the integral movement is in the direction of the lower concentration until an equilibrium is reached. The concentration profile dissolves with time forming a Gaussian distribution with variance $\sigma(t) = \sqrt{Dt}$ [8] .

Drift is caused by an externally applied electrical field. In that case the carriers move along the field lines. In a sensor with a high applied field the diffusion contribution is negligible.

Drift velocity $v_{\text{drift}}(E)$ is the speed at which the charge carriers drift through the diamond sensor [8].

Mobility μ is a proportionality factor between the v_{drift} and the electric field E at low electric fields: $v_{\text{drift}} = \mu E$. Its units are in $\text{cm}^2 \text{ V}^{-1} \text{ s}^{-1}$.

Phonon transport is the transfer of energy of the moving charges to the lattice.

Saturation velocity v_{sat}^e is a velocity limit above which the carriers cannot reach. This is due to increasing phonon transport at a high electric field. The $v_{\text{sat}}^e = v_{\text{sat}}^h = (14.23 \pm 0.12) \times 10^6 \text{ cm/s}$ for both positive and negative charge carriers has been derived from the measurements in [13].

The final equation for v_{drift} is therefore [14]

$$v_{\text{drift}}(E) = \mu(E)E = \frac{\mu_0 E}{1 + \frac{\mu_0 E}{v_{\text{sat}}}}. \quad (1.10)$$

It can be retrieved experimentally via the transit time measured with the Transient Current Technique (TCT). This technique enables the measurement of transit time t_t of the carriers through the sensor with the thickness d .

$$v_{\text{drift}}(E) = \frac{d}{t_t(E)}. \quad (1.11)$$

The velocities for holes and electrons usually differ. In diamond, the holes travel approximately 30 % faster than electrons at the room temperature [12].

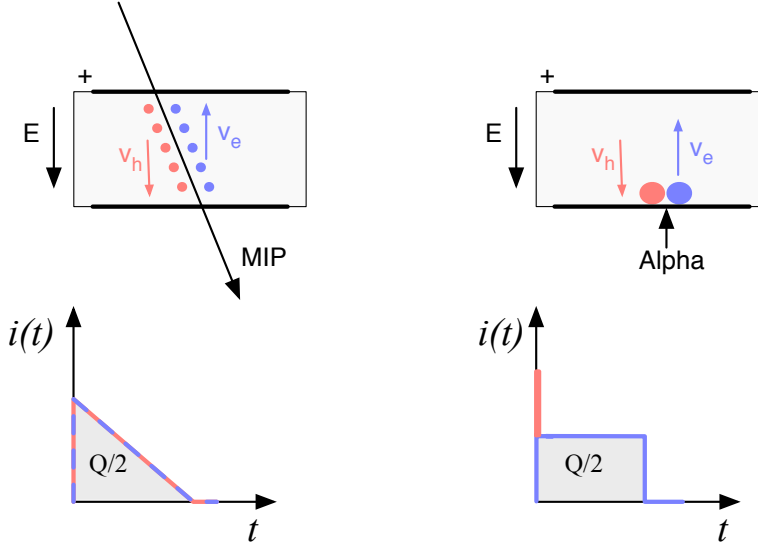


Figure 1.6: Charge carrier drift in diamond for β and for α particles crossing the sensor at $t = 0$.

225 1.4 Radiation-induced current signals

226 When a highly-energetic particle travels through the sensor, it interacts with atoms in the
 227 lattice. It ionises the valence electrons, creating electron-hole (e-h) pairs on its way. It can
 228 either deposit only a fraction of its energy and exit the sensor on the other side or it can get
 229 stopped in the sensor, depositing all of its energy. A special case is when it interacts with the
 230 core of the atom in the middle of the sensor by means of a nuclear interaction. All these
 231 various types interactions produce different amounts and different spatial distributions of
 232 e-h pairs.

233 The two most frequent types are shown in figure 1.6. The first figure shows the inter-
 234 action of an incident MIP. The electrons and holes created all along the trajectory of the
 235 particle immediately start drifting towards the positive and negative electrode, respectively.
 236 At $t = 0$ all charges drift, contributing to the maximum induced current. Those closest to
 237 the electrodes have a very short drift path. They stop inducing current upon reaching the
 238 electrode. The resulting current signal is a triangular pulse with a sharp rising edge and a
 239 linear falling edge. Gradually all the charge carriers reach the electrode. The accumulated
 240 charge Q_s equals to the sum of the contributions of the positive and negative charge carriers.

241 The second type of interaction happens when the particle is stopped in the diamond
 242 close to the point of entry. Most of its energy is deposited in a small volume close to the
 243 electrode. A cloud of charge carriers is created and the charges with the shorter path to the
 244 electrode disappear almost instantly. The carriers of the opposite charge, however, start
 245 drifting through the sensor to the other electrode. In an ideal diamond sensor, their velocity
 246 is constant throughout the drift up until they are collected at the opposite electrode. The
 247 contribution of the first charge cloud is a peak with a short time. The cloud drifting through

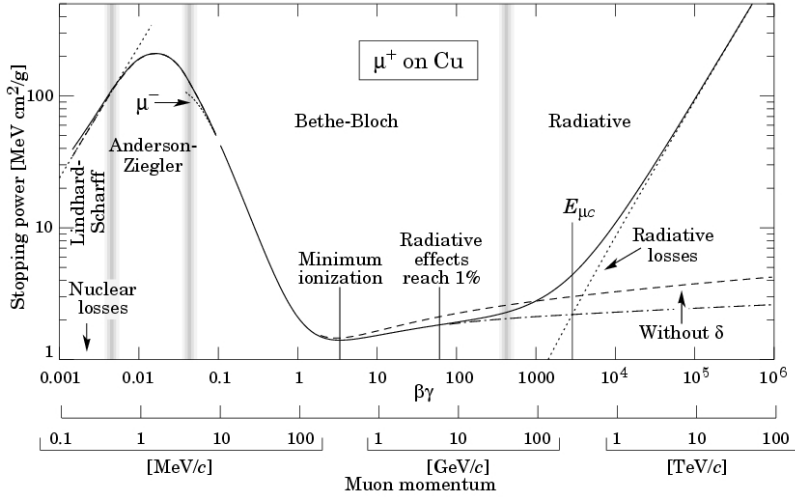


Figure 1.7: Stopping power for muons according to the Bethe-Bloch formula [15].

the sensor, on the other hand, induces a current signal with a flat top. The resulting signal has a shape of a rectangle, with a spike in the beginning. The accumulated charge Q_s is equal to a half of the deposited charge by the stopped particle.

The two aforementioned types of interactions have well defined signal responses. Nuclear interactions on the other hand yield various results. The resulting signal shape depends on the decay products of the interaction, which can be α , β or γ quanta or other nuclei, inducing a mixed shaped signal.

1.4.1 Mean energy loss

A mean energy loss of a particle traversing the detector as a function of the momentum is given with the Bethe-Bloch equation [15]:

$$-\left\langle \frac{dE}{dx} \right\rangle = \frac{4\pi}{m_e c^2} \cdot \frac{nz^2}{\beta^2} \cdot \left(\frac{e^2}{4\pi\epsilon_0} \right)^2 \cdot \left(\ln \left(\frac{2m_e c^2 \beta^2}{I \cdot (1 - \beta^2)} \right) - \beta^2 \right) \quad (1.12)$$

The resulting function for a muon is shown in figure 1.7. At a momentum of around 300 MeV/c the incident particle deposits the lowest amount of energy. Hence it is referred to as the *minimum ionising particle* or a MIP.

1.4.2 Signal fluctuation

Two important sensor properties are the magnitude of the signal and the fluctuations of the signal at a given absorbed energy. They determine the relative resolution $\Delta E/E$. For semiconductors the signal fluctuations are smaller than the simple statistical standard deviation $\sigma_Q = \sqrt{N_Q}$. Here N_Q is the number of released charge pairs, i.e. the ratio between the total deposited energy E_0 and the average energy deposition E_i required to produce an electron-hole pair. [16] shows that the standard deviation is $\sigma_Q = \sqrt{F N_Q}$, where F is the

1.4. RADIATION-INDUCED CURRENT SIGNALS

268 Fano factor [16] (0.08 for diamond and 0.115 for silicon [17]). Thus, the standard deviation
269 of the signal charge is smaller than expected, $\sigma_Q \approx 0.3\sqrt{N_Q}$. The resulting intrinsic
270 resolution of semiconductor detectors is

$$\Delta E_{\text{FWHM}} = 2.35\sqrt{FEE} \quad (1.13)$$

271 wherein $E_i(Si) = 3.6$ eV and $E_i(Di) = 13$ eV. E.g., for an α particle with energy $E_\alpha = 5.5$
272 MeV the calculated resolution in diamond is equal to $\Delta E_{\text{FWHM}} = 5.6$ keV. This defines the
273 minimum achievable resolution for energy spectroscopy with semiconductors.

274 1.4.3 Charge collection

275 The total measured charge Q_i is the integral of the induced current:

$$Q_i = \int i_{\text{ind}}(t)dt. \quad (1.14)$$

276 The expected charge Q_0 can be calculated using the thickness of the sensor d and the
277 average number of e-h pairs created per μm δ_d , which is 36 e-h/ μm for diamond according
278 to table 1.1. The expected charge created by a MIP flying through a sensor with a thickness
279 $d = 500$ μm perpendicular to the electrodes is

$$Q_{\text{MIP}} = \delta_d \cdot d \cdot q = 18 \times 10^3 \text{ eh} \cdot q = 2.9 \text{ fC} \quad (1.15)$$

280 where $q = 1.6 \times 10^{-19}$ C is the elementary charge. If a particle stops in the sensor, it
281 deposits all its energy. In this case the number of created e-h pairs is calculated according
282 to equation 1.16 using E_{eh} , the energy required to create an e-h pair. For diamond this
283 value is 13, according to table 1.1. For a 5.5 MeV α particle emitted from an ^{241}Am source
284 the expected charge is

$$Q_\alpha = \frac{E}{E_{\text{e-h}}} \cdot q = \frac{5.5 \text{ MeV}}{13 \text{ eV}} \cdot q = 4.25 \times 10^5 \text{ eh} \cdot q = 68 \text{ fC}. \quad (1.16)$$

285 where E is the energy of the incident particle, which is almost for a factor of 24 larger than
286 expected charge of a MIP. The charge collection efficiency (CCE) is the ratio between the
287 measured and expected charge:

$$CCE = \frac{Q_i}{Q_0} = \frac{Q_i}{\delta_d \cdot d} \cdot 100\%. \quad (1.17)$$

288 The charge collection distance (CCD) is a measure of an average path that the charge
289 carriers travel before getting trapped:

$$CCD = \frac{Q_i}{\delta_d} \quad (1.18)$$

290 and is usually given in units of μm .

291 Carriers that get trapped stop contributing to the overall induced current on the elec-
292 trodes. The more charges are trapped along their drift path, the more the current induced
293 on the electrodes is decreased. This in turn yields a lower integrated charge. An expected

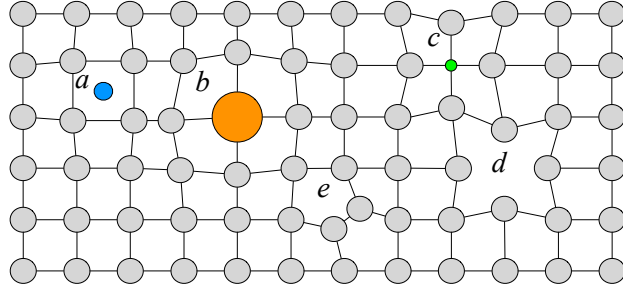


Figure 1.8: Impurities and non-uniformities in the crystal lattice due to radiation damage.

294 CCE for non-irradiated sCVD diamonds is close to 100 %. For highest quality non-irradiated
 295 pCVD diamonds it ranges between 40 % and 60 %. In other words, high-quality pCVD
 296 diamonds already have traps introduced by means of grain boundaries, which are created in
 297 the growing process. Traps can also be created by damaging the diamond using radiation
 298 (discussed in section 1.5). The more the sensor is irradiated, the larger number of traps is
 299 introduced in the material and the higher is the probability that the carriers are stopped
 300 on the way, reducing in turn the integrated charge. Therefore the CCD and CCE can be
 301 used as a means to quantify the detector damage due to radiation.

302 1.4.4 Charge trapping

303 Various types of lattice defects can be created in diamond, similar to those in silicon [18].
 304 Figure 1.8 shows several examples of lattice damage:

- 305 a) foreign interstitial (e.g. H, Li),
- 306 b, c) foreign substitutional (e.g. N, P, B),
- 307 d) vacancy and
- 308 e) self interstitial.

309 These non-uniformities form new energy levels in the forbidden gap. These intermediate
 310 levels are referred to as charge traps because they can trap moving charge carriers. The
 311 energy level of the trapped carriers is reduced from the conduction band to the energy level of
 312 the trap. Different types of lattice damage have different energy levels. The carriers trapped
 313 in a shallow trap – an energy level close to the conduction band – have a high probability
 314 of being thermally excited back into the conduction band whereby they continue drifting
 315 towards the electrode. Their activation energy is therefore low. Those trapped in a deep
 316 trap close to the middle of the forbidden gap need a much higher activation energy, which
 317 in turn increases the average time to their release due to thermal excitation.

318 The energy band jumping goes the other way, too. The carriers in the valence band may
 319 use the intermediate energy levels as “stepping stones” to jump to the conduction band and
 320 start drifting in the externally applied electric field. These intermediate energy levels are
 321 referred to as the generation centres of leakage current.

322 The charge carriers that drift through the bulk get stopped in the charge traps with a
 323 certain probability. This trapping happens uniformly throughout the diamond. In other
 324 words, the number of carriers in the moving charge cloud is gradually reduced. This in turn
 325 reduces the induced current. The number of drifting carriers per unit of length follows a
 326 decaying exponential function

$$I(t) = I_0 + I(0) \cdot e^{-\frac{t-t_0}{\tau}}, \quad (1.19)$$

327 where $I(0)$ is the initial induced current, I_0 is the end current, t is time, t_0 is temporal
 328 displacement of the pulse and τ is the decay time constant. This value describes how long
 329 it takes before the amplitude of the pulse decreases to 63 % of its initial height.

330 Priming/pumping

331 Priming or pumping [19] is a process of irradiating the diamond with ionising radiation
 332 with a goal to improve the sensor properties. The pumping process strongly reduces the
 333 concentration of active carrier trapping centres. This leads to an enhancement of electronic
 334 properties of such material. The improved transport properties due to a reduced number
 335 of active charge traps give rise to an increased charge collection efficiency. The diamond is
 336 usually pumped for a few hours using a strong β source, preferably a ^{90}Sr source with the
 337 activity of at least 50 MBq. The diamond remains in a pumped state from a few minutes
 338 to several days, depending on the quality of the material. A direct exposure to light results
 339 in an immediate return to an non-pumped state.

340 1.5 Radiation damage

341 Exposure to ionising radiation degrades sensors by deforming the crystal lattice and intro-
 342 ducing charge traps in the material.

343 Radiation damage varies with the type of radiation and its energy. There are several
 344 models existing [20, 21] that try to explain the impact of irradiation and to provide *damage*
 345 *factors* to compare the radiation damage between different particles. The standard way is
 346 to convert the damage into *1 MeV neutron equivalent fluence* [22]. Some models have been
 347 extensively verified with simulations and with experiments. In these experiments the charge
 348 collection in sensors is measured before and after irradiation. This procedure is repeated
 349 several times, with a measurement point taken after every irradiation. Then the charge
 350 collection for this set of measurements is plotted as a function of the radiation dose received
 351 by a specific particle at a specific energy. From this a damage factor k_λ can be extracted.
 352 Damage factors have to be measured across a range of energies and types of radiation to
 353 properly quantify the damage in the sensors. Finally they are compared to the simulations
 354 to validate the theoretical models.

355 Diamond is an expensive material and the technology is relatively new as compared to
 356 silicon. Therefore few institutes are carrying out diamond irradiation studies. To join the
 357 efforts, the RD42 collaboration [23] has been formed. It gathers the experimental data from
 358 diamond irradiation studies. Unlike with silicon, the experimental results so far show no
 359 significant correlation with the NIEL (non-ionising energy loss) model [20], which correlates

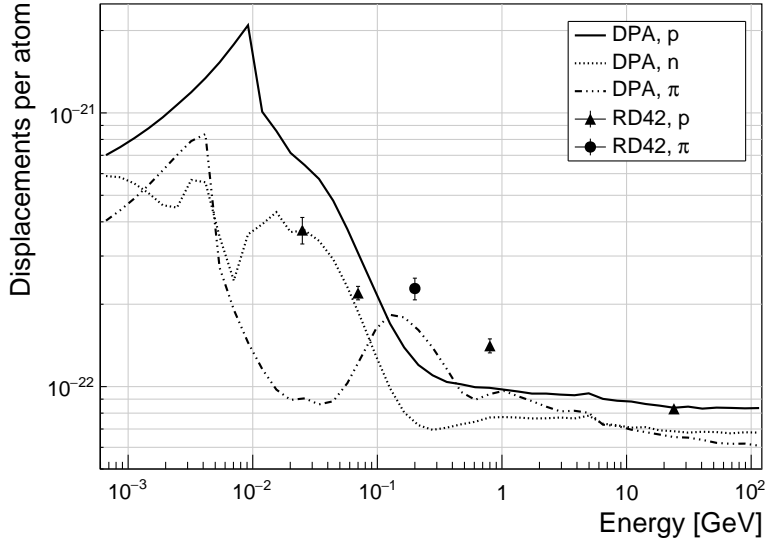


Figure 1.9: Diamond radiation damage - a model based on displacements per atom [21]. The figure shows the DPA as a function of the kinetic energy for protons, neutrons and pions. Added are data points for protons and pions by RD42 [24].

detector efficiency with the number of lattice displacements. Therefore an alternative model was proposed [21], correlating the diamond efficiency with the number of displacements per atom (DPA) in the material. The idea is that if the recoil energy of an incident particle is higher than the lattice binding energy (42 eV for diamond), the atom is displaced from its original position. The newly formed vacancy acts as a trap for drifting charge carriers. The more displacements that form in the crystal, the higher is the probability that a drifting carrier gets trapped. However, different types of particles interact differently with the material. In addition the mechanisms of interaction at low energies are different to those at high energies. To assess the damage for individual particles at a range of energies, simulations need to be run first. The simulation shown in [21] shows the DPA model for a range of energies of proton, pion and neutron irradiation in diamond. Figure 1.9 contains the simulation results as well as the superimposed empirical results of several irradiation studies. According to the figure, a 300 MeV pion beam damages the diamond material twice as much as a 24 GeV proton beam. The data points obtained by RD42 are also added to the figure. They have been normalised to damage by 24 GeV protons. This value has been chosen because radiation damage at this energy and radiation type is well understood at CERN.

377 Irradiation damage factor

378 The irradiation damage factor k_λ is a means to quantify irradiation damage of a specific
 379 type of radiation at a specific energy. Via this factor different types of irradiation can be
 380 compared. It is obtained experimentally by measuring the CCD of a number of samples at
 381 various irradiation steps and fitting the equation 1.20 to the data. λ is the measured CCD,

1.6. TEMPERATURE EFFECTS

³⁸² λ_0 is the CCD of a non-irradiated sample and Φ the radiation dose. As a reference, the
³⁸³ damage factor for 24 GeV protons is set to $1 \times 10^{-18} \mu\text{m}^{-1} \text{cm}^{-2}$.

$$\frac{1}{\lambda} = \frac{1}{\lambda_0} + k_\lambda \cdot \Phi \quad (1.20)$$

³⁸⁴ 1.6 Temperature effects

³⁸⁵ The band gap energy in diamond is equal to $E_g = 5.5 \text{ eV}$ while the average energy to produce
³⁸⁶ an electron-hole pair is $E_{e-h} = 13 \text{ eV}$. This means there is excessive energy deposited in
³⁸⁷ the diamond bulk. An incident α -particle stops within $\sim 10\text{--}15 \mu\text{m}$ of the bulk, transferring
³⁸⁸ all its energy to the lattice during deceleration. A part of this energy directly ionises the
³⁸⁹ carbon atoms, creating free electron-hole pairs.

³⁹⁰ The remaining energy, however, is converted into lattice vibrations – phonons [25, 12]. In
³⁹¹ other words, the lattice within the ionisation volume of approximately $\sim 15 \mu\text{m} \times \sim 2 \text{ nm}$ [12]
³⁹² is briefly heated up. The hot plasma then cools down to the temperature of the surrounding
³⁹³ material by means of heat dissipation, i.e. phonon transport.

³⁹⁴ The free electron binds with the free hole into a bound state (not recombination) –
³⁹⁵ the exciton [26]. The exciton binding energy is 80 meV, which introduces an energy level
³⁹⁶ within the forbidden gap just under the conduction band. At higher temperatures the
³⁹⁷ lattice provides enough energy to thermally excite the electron from the exciton state back
³⁹⁸ to the conduction band. At lower temperatures, however, the exciton lifetime increases,
³⁹⁹ which means that it takes a longer time for the electrons to get re-excited to the conduction
⁴⁰⁰ band. The re-excitation lifetime at room temperature is $\sim 30 \text{ ps}$, increasing to $\sim 150 \mu\text{s}$ at
⁴⁰¹ 50 K [12]. This means that some of the bound electrons do not even start drifting within
⁴⁰² the period of $\sim 10 \text{ ns}$, which is the expected carrier drift time. When they are finally freed,
⁴⁰³ the current they induce is already hidden in the electronics noise. The effective area of the
⁴⁰⁴ observed current pulse is therefore smaller than that of a pulse induced by all the carriers
⁴⁰⁵ drifting at the same time. This in effect reduces the measured collected charge. The longer
⁴⁰⁶ the time constant, the lower the measured collected charge, as shown in section 1.6.

⁴⁰⁷ Collected charge as a function of temperature

⁴⁰⁸ The area below the current pulse is proportional to the charge collected by the diamond
⁴⁰⁹ detector. The collected charge is measured as a function of temperature. First, the ampli-
⁴¹⁰ tude values of the averaged pulses at a bias voltage of $\pm 500 \text{ V}$ and across the temperature
⁴¹¹ range between 4 K and 295 K have to be integrated. Then a calibration factor is used to
⁴¹² derive the charge for all data points. The results of such measurements have been presented
⁴¹³ in [12]. Chapter ?? shows the results of the measurements taken in the scope of this thesis.

⁴¹⁴ 1.7 Electronics for signal processing

⁴¹⁵ This section describes the electronics of a detector, starting with a description of signal
⁴¹⁶ amplifiers and then discussing the digitisation and signal processing. All these stages are

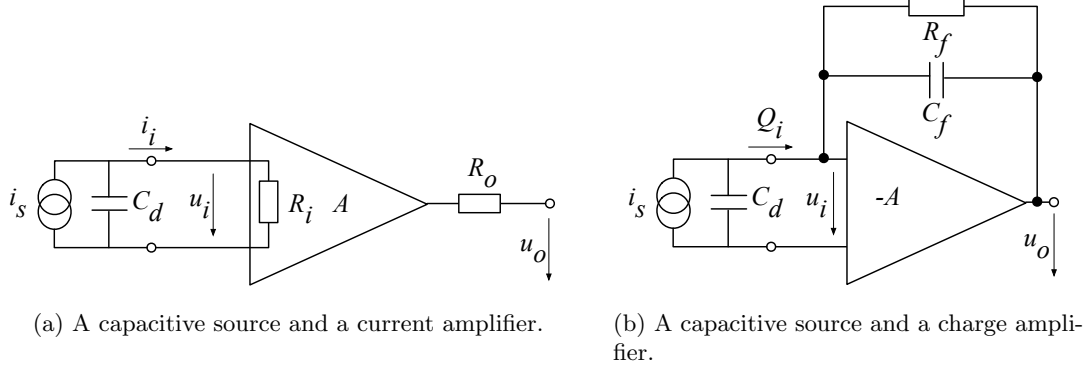


Figure 1.10: Simplified equivalent circuits of a current and charge amplifier.

417 necessary to extract information from the sensor. First, the signal has to be amplified.
 418 Then it is digitised and finally processed in a specially designed processor or a logic unit.

419 1.7.1 Signal preamplifiers

420 The signal charge generated in the sensor by a single energetic particle is of the order of a few
 421 fC. The range of the induced current for single particles is typically between 10^{-8} A (β, γ
 422 radiation) and 3×10^{-7} A (α radiation). Signals as low as these have to be pre-amplified
 423 before processing. Depending on the measurement, several types of signal amplifiers can
 424 be used. The preamplifiers are designed to minimise electronic noise while maximising
 425 gain, thus maximising the signal-to-noise ratio (SNR). In addition, a bandwidth limit must
 426 be optimised to minimise the information loss due to signal shape deformation. A critical
 427 parameter is the total capacitance, i.e. the sensor capacitance together with the capacitance
 428 load of the preamplifier. The SNR improves with a lower capacitance. Several types of
 429 amplifiers can be used, all of which affect the measured pulse shape. Two preamplifiers are
 430 used most commonly, a current and a charge sensitive amplifier. Both are described below.

431 Current amplifier

432 Figure 1.10a shows the equivalent circuit of a current source and a current amplifier. An
 433 amplifier operates in current mode if the source has a low charge collection time t_c with re-
 434 spect to the $R_i C_d$ time constant of the circuit. In this case the sensor capacitance discharges
 435 rapidly and the output current i_o is proportional to the instantaneous current i_i . The am-
 436 plifier is providing a voltage gain, so the output signal voltage u_o is directly proportional
 437 to the input voltage u_i :

$$u_o(t) = A \cdot R_i \cdot i_s(t). \quad (1.21)$$

438 The detector capacitance C_d together with the input resistance of the amplifier R_i defines
 439 the time constant of the signal, as shown in figure 1.11. The higher C_d , the slower is the
 440 response of the amplifier. For the case of the diamond sensor, which has the capacitance of
 441 the order of 2 pF and the input resistance of 50 Ω , the resulting time constant is $\tau = 10^{-10}$ s.
 442 This yields the signal rise time $t_r \sim 2.2\tau = 2.2 \times 10^{-10}$ s.

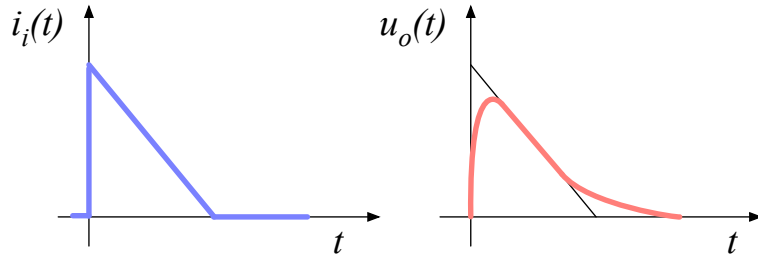


Figure 1.11: Input and output signal of the current amplifier.

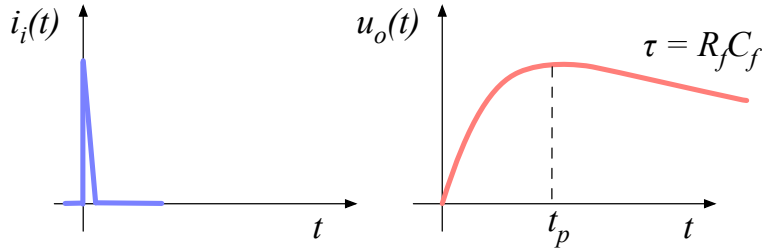


Figure 1.12: Input and output signal of the charge amplifier.

⁴⁴³ Charge-sensitive amplifier

⁴⁴⁴ In order to measure integrated charge in the sensor, a feedback loop is added to the amplifier,
⁴⁴⁵ as shown in figure 1.10b. The feedback can be used to control the gain and input resistance,
⁴⁴⁶ as well as to integrate the input signal. The charge amplifier is in principle an inverting
⁴⁴⁷ voltage amplifier with a high input resistance.

⁴⁴⁸ In an ideal amplifier the output voltage u_o equals $-Au_i$. Therefore the voltage difference
⁴⁴⁹ across the capacitor C_f is $u_f = (A + 1)u_i$ and the charge deposited on the capacitor is
⁴⁵⁰ $Q_f = C_f u_f = C_f(A + 1)u_i$. Since no current can flow into the amplifier, all of the signal
⁴⁵¹ current must charge up the feedback capacitance, so $Q_f = Q_i$.

⁴⁵² In reality, however, charge-sensitive amplifiers respond much slower than is the duration
⁴⁵³ of the current pulse from the sensor. In addition, a resistor is added to the feedback line in
⁴⁵⁴ parallel to the capacitor. The resistor and capacitor define the decay time constant of the
⁴⁵⁵ pulse, as shown in figure 1.12. This is necessary to return the signal to its initial state to
⁴⁵⁶ be ready for a new measurement.

⁴⁵⁷ Analogue electronic noise

⁴⁵⁸ The electronic noise determines the ability of a system to distinguish different signal levels.
⁴⁵⁹ The analogue signal contains ample information about the type and energy of incident
⁴⁶⁰ radiation, which can quickly be erased or altered if the signal properties change. Therefore
⁴⁶¹ the noise contributions to the signal must be well understood to qualify the information

462 the signal is carrying. The important contributions are listed below. Thermal or Johnson–
 463 Nyquist noise [27, 28] is the dominant noise contribution in the use case for diamond detector
 464 signal amplification and therefore defines the limitations of the detector system. This noise
 465 type is generated by the random thermal motion of charge carriers. The frequency range
 466 of the thermal noise is from 0 to ∞ with a predominantly uniform distribution. Therefore
 467 this is nearly a white noise. The resulting signal amplitude has a Gaussian distribution.
 468 The RMS of the open-loop equivalent voltage is defined as

$$u_{\text{RMS}} = \sqrt{4k_B RT \Delta f} \quad (1.22)$$

469 where k_B is the Boltzmann constant, R is the input resistance of the amplifier, T its tem-
 470 perature and Δf the frequency range. This equation shows that it is possible to reduce the
 471 noise RMS by either (1) reducing the frequency range, (2) reducing the resistance or (3)
 472 reducing the temperature.

473 Contributions of shot noise, flicker noise and burst noise and other types are not sig-
 474 nificant relative to the thermal noise. However, the contributions of external factors can
 475 severely deteriorate the signal. This means the noise produced by capacitive or inductive
 476 coupling with an external source, which causes interference in the signal. These effects can
 477 be reduced by shielding the electronics and avoiding ground loops.

478 1.7.2 Analogue-to-digital converters

479 An analogue-to-digital converter (ADC) is a device that converts the analogue electrical
 480 signal on the input to its digital representation - a series of digital values. This involves a
 481 quantisation – *sampling* of the signal at a defined sampling period, resulting in a sequence
 482 of samples at a discrete time period and with discrete amplitude values. The resolution
 483 of the ADC is the number of output levels the ADC can quantise to and is expressed in
 484 bits. For instance, an ADC with a resolution equal to $n = 8$ bit has a dynamic range of
 485 $N = 2^n = 256$ steps. The resulting voltage resolution Q_{ADC} at the input voltage range of
 486 $V_{\text{ADC}} = \pm 50$ mV is then

$$Q_{\text{ADC}} = \frac{V_{\text{ADC}}}{2^n} = \frac{100 \text{ mV}}{2^8 \text{ bit}} = 0.39 \text{ mV/bit.} \quad (1.23)$$

487 With a sampling period of $t_s = 1$ ns the sampling rate is $f_s = 1$ GS/s (gigasample per second).
 488

Quantisation error and quantisation noise (or a round-off error) is a contribution to the overall measurement error due to digitisation (rounding). The quantisation error is defined as a difference between the actual analog value and the closest digitised representation of this value, therefore by the least significant bit (LSB), as seen in figure 1.13. The input signal amplitude is typically much larger than the voltage resolution. In this case the quantisation error is not directly correlated with the signal and has an approximately uniform distribution. The probability density function $P(x)$ therefore has a rectangular shape bounded by $(-\frac{1}{2}\text{LSB}, \frac{1}{2}\text{LSB})$:

$$P(x) = \begin{cases} \frac{1}{\text{LSB}}, & -\frac{1}{2}\text{LSB} \leq x \leq \frac{1}{2}\text{LSB} \\ 0, & \text{otherwise.} \end{cases} \quad (1.24)$$

$$(1.25)$$

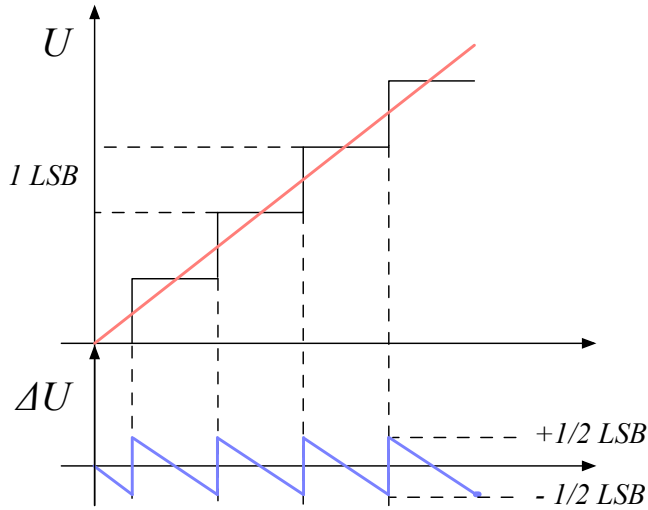


Figure 1.13: Input signal digitisation and quantisation error.

489 The height equal to $\frac{1}{\text{LSB}}$ preserves the integrated probability of 1. The variance of the
490 distribution is

$$\sigma^2 = \int P(x)(x - \mu)^2 dx. \quad (1.26)$$

491 The population mean is $\mu = 0$, therefore

$$\sigma^2 = \int_{-\frac{1}{2}\text{LSB}}^{\frac{1}{2}\text{LSB}} \frac{1}{\text{LSB}} x^2 dx = \frac{x^3}{3\text{LSB}} \Big|_{-\frac{1}{2}\text{LSB}}^{\frac{1}{2}\text{LSB}} = \frac{\text{LSB}^2}{12}. \quad (1.27)$$

492 The RMS of the quantisation noise is defined as the square root of the variance:

$$\Delta Q_{\text{ADC}} = \sqrt{\sigma^2} = \frac{1}{\sqrt{12}} \text{LSB} \sim 0.289 \text{ LSB}. \quad (1.28)$$

493 For the example above the quantisation error equals $\Delta Q_{\text{ADC}} = 0.11 \text{ mV}$. The error depends
494 strongly on the linearity of the ADC, but this is out of scope of this document as the devices
495 used have ADCs with a very good linearity.

496 1.7.3 Digital signal processing

497 The digitised signal can be processed to extract useful information. Therefore after the
498 signal amplification and digitisation the signal is routed in a device which handles the
499 digital analysis. The signal can either be processed immediately (in real time) or it can be
500 saved to a data storage for analysis at a later stage (offline). The devices carrying out the
501 processing can be multipurpose (e.g. Field Programmable Gate Arrays) or dedicated (e.g.
502 Application-Specific Integrated Circuits).

503 **Field Programmable Gate Array** (FPGA) is an integrated circuit designed to be re-
504 programmable and reconfigured after manufacturing. It consists of a set of logic gates that

505 can be interconnected in numerous combinations to carry out a set of logic operations.
506 Many such logic operations can take place in parallel, making the FPGA a powerful tool
507 for signal processing. FPGAs are often used during system development or in systems in
508 which the requirements might change with time. They can be reprogrammed in the order of
509 seconds. In addition, the logic design only needs minor changes when migrating to a newer
510 version of the FPGA chip of the same vendor. The FPGAs also offer faster time-to-market
511 with comparison to application-specific solutions, which have to be developed. On the other
512 hand, the price per part can be significantly higher than for the application-specific solu-
513 tions. Also, their other major disadvantages are a high power consumption and a relatively
514 low speed as compared to more application-specific solutions. However, today's solutions
515 are capable of clock speeds higher than 500 MHz. Together with the integrated digital
516 signal processing blocks, embedded processors and other modules, they are already very
517 powerful and versatile. All in all, FPGAs are a good choice for prototyping and limited
518 production, for projects with limited requirements for speed and complexity.

519 **Application-Specific Integrated Circuit** (ASIC) is an integrated circuit designed for
520 a specific use. The design cannot be modified after chip production, as is the case with
521 FPGAs. On the other hand, the ASICs can be optimised to perform a required operation
522 at a high speed and at a low power consumption. In addition, due to the specific design the
523 size of the chip can be much smaller. ASICs can be designed as hybrid chips, containing
524 both a digital and an analog part. Finally, ASICs can be designed to withstand much higher
525 irradiation doses than FPGAs and can therefore be used in harsh environments like in space
526 or in particle colliders.

527 To update the chip, the design has to be submitted to a foundry, which produces the new
528 chips with a turnover time of 4—6 weeks. The costs of a submission are high, but the
529 price per part can be reduced significantly with a high volume. To sum up, ASICs are used
530 for high volume designs with well defined requirements where some stringent constraints in
531 terms of power consumption and speed have to be met.

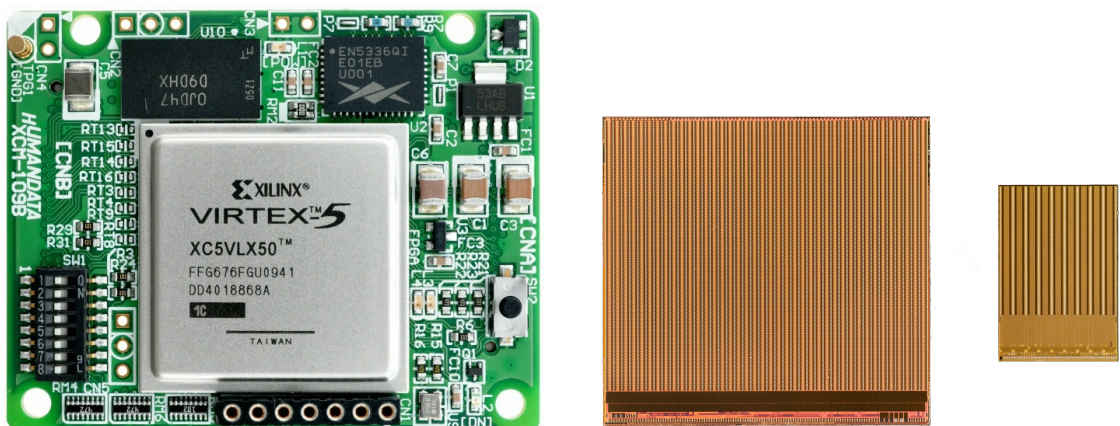


Figure 1.14: An example of a Xilinx Virtex 5 FPGA [29] and an FE-I4 and FE-I3 ASIC chip [30].

⁵³² Bibliography

- ⁵³³ [1] E. A. Ekimov, V. A. Sidorov, E. D. Bauer, N. N. Mel'nik, N. J. Curro, J. D. Thompson,
⁵³⁴ and S. M. Stishov. Superconductivity in diamond. *Nature*, 428(6982):542–545, 04 2004.
- ⁵³⁵ [2] 1951 Park, Jong-Hee, 1955 Sudarshan, T. S., and Inc ebrary. Chemical vapor de-
⁵³⁶ position. Materials Park, Ohio : ASM International, 2001. Includes bibliographical
⁵³⁷ references.
- ⁵³⁸ [3] CIVIDEC Instrumentation GmbH. *sCVD diamond sensor*. <http://www.cividec.at>,
⁵³⁹ 2015.
- ⁵⁴⁰ [4] Heinz Pernegger. *The Pixel Detector of the ATLAS Experiment for LHC Run-2*. Tech-
⁵⁴¹ nical Report ATL-INDET-PROC-2015-001, CERN, Geneva, Feb 2015.
- ⁵⁴² [5] Claudia Marcelloni De Oliveira. *IBL installation into the inner detector of the ATLAS*
⁵⁴³ *Experiment side C*. General Photo, May 2014.
- ⁵⁴⁴ [6] *Bremsstrahlung*. 2016.
- ⁵⁴⁵ [7] Yoshihiko Hatano, Yosuke Katsumura, and A. Mozumder. Charged Particle and Photon
⁵⁴⁶ Interactions with Matter: Recent Advances, Applications, and Interfaces. CRC
⁵⁴⁷ Press, 2010.
- ⁵⁴⁸ [8] S. Sze and K. N. Kwok. Physics of Semiconductor Devices, 3rd ed. Wiley, Hoboken,
⁵⁴⁹ NJ, 2007.
- ⁵⁵⁰ [9] W. Blum, W. Riegler, and L. Rolandi. Particle Detection with Drift Chambers, vol-
⁵⁵¹ ume 2 of *2*. Springer-Verlag, Berlin Heidelberg, 2008.
- ⁵⁵² [10] W. Shockley. *Currents to Conductors Induced by a Moving Point Charge*. *Journal of*
⁵⁵³ *applied Physics*, 9:635, 1938.
- ⁵⁵⁴ [11] S. Ramo. *Currents Induced by Electron Motion*. *Proceedings of the IRE*, 27:584–585,
⁵⁵⁵ 1939.
- ⁵⁵⁶ [12] Hendrik Jansen, Norbert Wermes, and Heinz Pernegger. *Chemical Vapour Deposition*
⁵⁵⁷ *Diamond - Charge Carrier Movement at Low Temperatures and Use in Time-Critical*
⁵⁵⁸ *Applications*. PhD thesis, Bonn U., Sep 2013. Presented 10 Dec 2013.

BIBLIOGRAPHY

- [559] [13] Hendrik Jansen, Daniel Dobos, Thomas Eisel, Heinz Pernegger, Vladimir Eremin, and
560 Norbert Wermes. Temperature dependence of charge carrier mobility in single-crystal
561 chemical vapour deposition diamond. *Journal of Applied Physics*, 113(17), 2013.
- [562] [14] Z. Li and H. Kraner. *Modeling and simulation of charge collection properties for neutron*
563 *irradiated silicon detectors. Nuclear Physics B - Proceedings Supplements* 32, (32):398–
564 409, 1993.
- [565] [15] Peter Sigmund. Particle Penetration and Radiation Effects Volume 2 - General Aspects
566 and Stopping of Swift Point Charges, volume 151 of *Springer Series in Solid-State*
567 *Sciences*. Springer-Verlag Berlin Heidelberg, 2006.
- [568] [16] U. Fano. Ionization Yield of Radiations. II. The Fluctuations of the Number of Ions.
569 *Physical Review*, 72:26–29, July 1947.
- [570] [17] R. C. Alig, S. Bloom, and C. W. Struck. Scattering by ionization and phonon emission
571 in semiconductors. 22:5565–5582, December 1980.
- [572] [18] Claude A. Klein. Radiation-induced energy levels in silicon. *Journal of Applied Physics*,
573 30(8):1222–1231, 1959.
- [574] [19] Marco Marinelli, E. Milani, M. E. Morgada, G. Pucella, G. Rodriguez, A. Tuccia-
575 rone, G. Verona-Rinati, M. Angelone, and M. Pillon. Thermal detrapping analysis of
576 pumping-related defects in diamond. *Applied Physics Letters*, 83(18):3707–3709, 2003.
- [577] [20] M. Huhtinen. *Simulation of non-ionising energy loss and defect formation in sili-*
578 *con. Nuclear Instruments and Methods in Physics Research A*, 491:194–215, September
579 2002.
- [580] [21] Moritz Guthoff, Wim de Boer, and Steffen Mller. Simulation of beam induced lat-
581 tice defects of diamond detectors using {FLUKA}. *Nuclear Instruments and Methods in Physics*
582 *Research Section A: Accelerators, Spectrometers, Detectors and Associated Equipment*, 735:223 – 228, 2014.
- [584] [22] Determination of operational dose equivalent quantities for neutrons. ICRU, Wash-
585 ton, DC, 2001.
- [586] [23] RD42 collaboration. <http://rd42.web.cern.ch/rd42/>.
- [587] [24] M. Mikuž. *Diamond sensors for high energy radiation and particle detection*. TIPP,
588 2011.
- [589] [25] J. L. Yarnell, J. L. Warren, and R. G. Wenzel. Lattice vibrations in diamond. *Phys.*
590 *Rev. Lett.*, 13:13–15, Jul 1964.
- [591] [26] W. Y. Liang. Excitons. *Physics Education*, 5:226–228, July 1970.
- [592] [27] J. B. Johnson. *Thermal Agitation of Electricity in Conductors*. *Phys. Rev.*, 32:97–109,
593 Jul 1928.

BIBLIOGRAPHY

- 594 [28] H. Nyquist. *Thermal Agitation of Electric Charge in Conductors.* *Phys. Rev.*, 32:110–
595 113, Jul 1928.
- 596 [29] Xilinx Virtex 5 FPGA. <http://www.hdl.co.jp/XCM-109/top.560.jpg>.
- 597 [30] M. Garcia-Sciveres. ATLAS Experiment Pixel Detector Upgrades. 2011.